








Chiral phonons and phononic birefringence in ferromagnetic metal–bulk acoustic resonator hybridsM. Müller ^{1,2,*} J. Weber,^{1,2} F. Engelhardt ^{3,4,5} V. A. S. V. Bittencourt,⁶ T. Luschmann,^{1,2,7} M. Cherkasskii ⁵ M. Opel ¹
S. T. B. Goennenwein,⁸ S. Viola Kusminskiy ^{5,3} S. Geprägs,¹ R. Gross ^{1,2,7} M. Althammer,^{1,2,†} and H. Huebl ^{1,2,7,‡}¹Walther-Meißner-Institut, Bayerische Akademie der Wissenschaften, 85748 Garching, Germany²Technical University of Munich, TUM School of Natural Sciences, Physics Department, 85748 Garching, Germany³Max Planck Institute for the Science of Light, 91058 Erlangen, Germany⁴Department of Physics, University Erlangen-Nuremberg, 91058 Erlangen, Germany⁵Institute for Theoretical Solid State Physics, RWTH Aachen University, 52074 Aachen, Germany⁶ISIS (UMR 7006), Université de Strasbourg, 67000 Strasbourg, France⁷Munich Center for Quantum Science and Technology (MCQST), 80799 Munich, Germany⁸Department of Physics, University of Konstanz, 78457 Konstanz, Germany

(Received 15 March 2023; revised 25 August 2023; accepted 19 December 2023; published 23 January 2024)

Magnomechanical devices, in which magnetic excitations couple to mechanical vibrations, have been discussed as efficient and broadband microwave signal transducers in the classical and quantum limit. We experimentally investigate the resonant magnetoelastic coupling between the ferromagnetic resonance modes in metallic $\text{Co}_{25}\text{Fe}_{75}$ thin films, featuring ultralow magnetic damping as well as sizable magnetostriction, and standing transverse elastic phonon modes in sapphire, silicon, and gadolinium gallium garnet at cryogenic temperatures. For all substrates, we observe a coherent interaction between the acoustic and magnetic modes. We identify the phonon modes as transverse shear waves propagating with slightly different velocities ($\Delta v/v \simeq 10^{-5}$); i.e., all investigated substrates show potential for phononic birefringence as well as phonon-mediated angular momentum transport. Our magnon-phonon hybrid systems operate in a coupling regime analogous to the Purcell enhanced damping in cavity magnonics.

DOI: [10.1103/PhysRevB.109.024430](https://doi.org/10.1103/PhysRevB.109.024430)**I. INTRODUCTION**

Phonons, the quantized excitations of elastic waves in solids, are a crucial concept for a vast variety of solid-state phenomena. Recently, they came into focus in the field of quantum science due to potential applications in quantum memories [1–4], quantum transducers [5–10], and quantum sensors [11–15]. In this context, the research mainly focuses on standing elastic wave patterns in mechanical resonators with high quality factors [16,17] which can be realized, e.g., in the form of high-order harmonic overtone bulk acoustic wave (BAW) [18,19] or surface acoustic wave (SAW) resonators [1,2,20,21]. These resonators support both longitudinal and transverse (shear) elastic standing waves, typically with linear polarization. However, superpositions of phonons based on shear waves have the ability to also carry angular momentum. This could enable the transfer or storage of angular momentum as well as the conversion between circularly polarized and linearly polarized shear waves, allowing for the realization of phononic spin valves [22,23]. Magnons, the quantized excitations of magnets, are ideal sources of phonons with a defined chirality, as they couple to phonons via the spin-orbit interaction whereas the sense of the magnetic

precession is determined by the sign of the gyromagnetic ratio [22–33]. Regarding suitable material platforms, bulk acoustic resonators with high quality factors combined with magnetic materials with low magnon damping and strong spin-orbit interaction are promising for the realization of magnon-phonon hybrids. Early experiments [22,23,28] focused on the ultra-low-magnetization damping material yttrium iron garnet ($\text{Y}_3\text{Fe}_5\text{O}_{12}$, YIG) grown lattice matched on gadolinium gallium garnet ($\text{Gd}_3\text{Ga}_5\text{O}_{12}$, GGG) substrates. However, the constraint to GGG substrates is far from ideal as GGG has unfavorable acoustic and magnetic properties especially at low temperatures. For the investigation of angular momentum transport and phononic birefringence in quantum acoustics and spintronics, the following aspects need addressing: (i) enable the use of low-acoustic-damping materials, e.g., sapphire and silicon, which are compatible with low-temperatures and quantum applications; (ii) gain quantitative understanding of the impact of the crystal symmetry on the propagation properties of chiral phonons to foster angular momentum transport and allow for tailored experiments on phononic birefringence; and (iii) gain access to a large variety of substrate materials with a plethora of crystal symmetries via suitable magnetic thin films that do not require epitaxy for the excitation of chiral phonons.

Here, we address all of these aspects and demonstrate that polycrystalline metallic magnetic thin films are well suited for the excitation of high-overtone BAWs in sapphire (Al_2O_3), silicon (Si), and GGG. This provides clear evidence that the

*manuel.mueller@wmi.badw.de

†matthias.althammer@wmi.badw.de

‡hans.huebl@wmi.badw.de

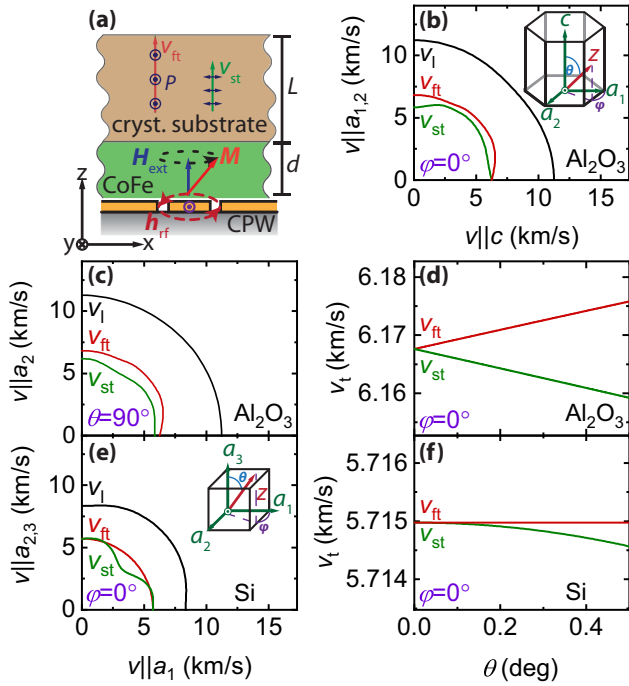


FIG. 1. (a) Schematic of the sample composed of a metallic CoFe thin film on a crystalline substrate mounted on a coplanar waveguide. The transverse acoustic waves can split into fast and slow modes with velocities v_{ft} and v_{st} , respectively (red and green arrows), and different polarization directions \mathbf{P} (blue arrows). (b) Group velocities of the longitudinal and transverse acoustic phonons of hexagonal Al_2O_3 in the $\mathbf{a}_{1,2}\text{-c}$ plane showing the velocity dependence with respect to the propagation direction of the phonons. The inset defines the phonon propagation direction \mathbf{z} with respect to the crystallographic axes of Al_2O_3 . (c) Phonon group velocities of Al_2O_3 in the $\mathbf{a}_1\text{-a}_2$ plane for $\theta = 90^\circ$. (d) Calculated splitting of the slow and fast transverse mode velocities v_{st} and v_{ft} in Al_2O_3 as a function of θ ($\varphi = 0^\circ$). (e) Group velocities of the longitudinal and transverse acoustic phonons of cubic Si in the $\mathbf{a}_1\text{-a}_{2,3}$ plane. The vector \mathbf{z} defines the phonon propagation direction with respect to the cubic lattice vectors \mathbf{a}_i . (f) Calculated splitting of v_{st} and v_{ft} in Si for $\varphi = 0^\circ$ as a function of θ .

elastic excitation scheme is generic. We extract this information from the resonant interaction of the ferromagnetic excitations with the standing elastic waves from the BAWs. We find that at least two propagation velocities must be considered in our substrates, suggesting that the phonon propagation direction with respect to crystallographic axes is of key importance to carry angular momentum and to convert chiral to linearly polarized phonons. Moreover, our experiments at 5 K indicate that this platform could be developed further towards the quantum regime.

II. QUALITATIVE DISCUSSION

We consider ferromagnetic metallic (FM) $\text{Co}_{25}\text{Fe}_{75}$ (CoFe) thin films deposited on crystalline substrates [see Fig. 1(a)]. When subjected to a sufficiently large magnetic field H_{ext} the magnetization \mathbf{M} of the CoFe is oriented along the film normal (\mathbf{z} direction), parallel to H_{ext} . Using ferromagnetic resonance (FMR) techniques, we drive the Kittel mode, whose frequency

depends on H_{ext} . Due to the finite magnetoelastic coupling (MEC) [22,23,28,34,35], the magnetization dynamics generates a high-frequency stress field and hence elastic modes with the same frequency and helicity as the magnonic mode. As the magnetic thin film is elastically coupled to the substrate, the elastic modes (phonons) can also propagate therein. This process is called phonon pumping [29]. For the geometry chosen in Fig. 1(a), the excited phonons are exclusively the transverse acoustic phonons as the projection of the magnetization vector \mathbf{M} on the field direction is constant in the linear response regime and hence no longitudinal acoustic phonons are generated along the out-of-plane direction \mathbf{z} [29,30]. Due to our experimental setting with a thin magnetic film acting as a transducer on top of a substrate, the properties of the standing waves are dominated by the phonon dispersion relation of the substrate material, which depends on the details of the substrate's crystal structure [36–38]. The excited phonons have wave numbers close to the center of the Brillouin zone, where the dispersion relation is to a good approximation linear, and, hence, group and phase velocities are identical. However, depending on the symmetry of the crystal, these velocities are usually anisotropic; i.e., they depend on the propagation direction (\mathbf{z} direction in our setting) relative to the crystallographic axis [cf. Fig. 1(b)], as described by the Christoffel equation [39,40]. Figures 1(b) and 1(c) show the calculated phonon propagation velocities solving the Christoffel equation [40] for the exemplary case of hexagonal Al_2O_3 [41], where the anisotropy of the velocities reflects the symmetry of the underlying crystal structure. For shear waves with a propagation direction \mathbf{z} along the hexagonal \mathbf{c} direction, the velocities of fast and slow transverse phonon modes, v_{ft} and v_{st} , are identical. However, if \mathbf{z} is not parallel to the \mathbf{c} axis, this degeneracy is lifted even for small angles θ between \mathbf{z} and \mathbf{c} as displayed in Fig. 1(d). Moreover, for small θ values, the θ dependence of v_{ft}/v_{st} cannot be neglected. This lifting of degeneracy for v_{ft} and v_{st} is not unique to hexagonal crystals. Figures 1(e) and 1(f) show the corresponding phonon velocity anisotropy for small θ in Si (diamond structure) [42].

As depicted in Fig. 1(a), the propagating phonons meet reflective boundary conditions imposed by the finite thickness $L + d \simeq L$ of the sample composed of substrate (L) and magnetic thin film (d). This leads to the formation of standing waves. For $L \simeq 510 \mu\text{m}$, this corresponds to a mode spacing in the megahertz range for transverse acoustic modes propagating with velocities $\simeq 6 \text{ km/s}$. As we excite the FMR in the CoFe layer at gigahertz frequencies, we operate this BAW resonator in the high-overtone regime. Here, the resonance frequency of an elastic standing wave mode with mode number n can be well approximated by [30]

$$f_{n,i} = n/[2(d/\tilde{v}_t + L/v_i)]. \quad (1)$$

Here, $i = \text{st}, \text{ft}$ and the transverse phonon velocity of the magnetic thin film is \tilde{v}_t . Whenever the frequency of the FMR is resonant with one of the standing wave modes of the BAW, we excite the elastic mode via MEC. This results in a change of the FMR signature due to phonon pumping [29,30] at f_n and thus yields a frequency-periodic modification of the FMR, where the periodicity is given by the free spectral range $f_{\text{FSR},i} = f_{n+1,i} - f_{n,i} = f_{1,i}$ [22,23,28]. Note that the FMR

TABLE I. Parameters for plot in Fig. 3(a). Frequency f_0 , resonance field $\mu_0 H_{\text{res}}$, as well as minimum and maximum S_{21} parameter, $\min(|S_{21}|)$ and $\max(|S_{21}|)$.

f_0 (GHz)	12	18	24	30
$\mu_0 H_{\text{res}}$ (T)	2.80	3.01	3.21	3.42
$\min(S_{21})$ (10^{-3})	55	16	5.1	2.2
$\max(S_{21})$ (10^{-3})	75	26	8.6	4.0

absorption line is sensitive to all elastic modes, which can be excited with the stress field created via MEC in the FM film.

Due to imperfections in the cutting and polishing process, present in realistic substrates, the surface normal is typically not perfectly aligned parallel to the c axis but may slightly deviate from it by a miscut angle θ_m , which denotes the angle between the surface normal \mathbf{z} and the respective crystallographic axis. Therefore, we expect the observation of nondegenerate propagation velocities v_{ft} and v_{st} along \mathbf{z} . This manifests as a superposition of the frequency periodic FMR signature with the respective free spectral range $f_{1,i}$, which can be resolved if the phononic linewidths are sufficiently narrow. In this case, the group velocities of the excited acoustic phonon modes can be determined using Eq. (1). Thus, FMR can be considered a technologically simple, but sensitive, tool for the investigation of excitations in BAW resonators.

III. EXPERIMENTAL RESULTS

We deposit a Pt (3 nm)/Cu (3 nm)/CoFe (30 nm)/Cu (3 nm)/Ta (3 nm) multilayer stack via dc magnetron sputtering on a 510- μm -thick (0001)-oriented Al_2O_3 substrate, a 675- μm -thick (001)-oriented high-resistivity Si substrate, and a 380- μm -thick (111)-oriented GGG substrate, which are all polished on both sides. The seed layer of the CoFe film is composed of a Pt (3 nm)/Cu (3 nm) bilayer which is sufficiently thin to maintain good elastic coupling between the substrates and the CoFe layer and ensures optimal magnetization damping of (110)-textured CoFe thin films [43–45] (see Appendix A 6). The top Cu (3 nm)/Ta (3 nm) layers prevent oxidation of the CoFe thin film. To analyze the MEC, we perform broadband FMR experiments in a magnet cryostat [46]. The sample is mounted face down onto a coplanar waveguide and we record the frequency-dependent complex microwave transmission parameter S_{21} as a function of the out-of-plane magnetic field H_{ext} using a vector network analyzer.

A. Magnon-phonon interaction

Figure 2(a) shows $|S_{21}|$ as a function of H_{ext} and microwave frequency f around $f_0 = 18$ GHz recorded at $T = 5$ K for

TABLE II. Parameters for plot in Fig. 3(b). Frequency f_0 and corresponding resonance field $\mu_0 H_{\text{res}}$ as well as minimum and maximum S_{21} parameter, $\min(|S_{21}|)$ and $\max(|S_{21}|)$.

f_0 (GHz)	20.5	21	21.5	22
$\mu_0 H_{\text{res}}$ (T)	3.09	3.10	3.12	3.13
$\min(S_{21})$ (10^{-3})	39	36	31	32
$\max(S_{21})$ (10^{-3})	55	51	44	45

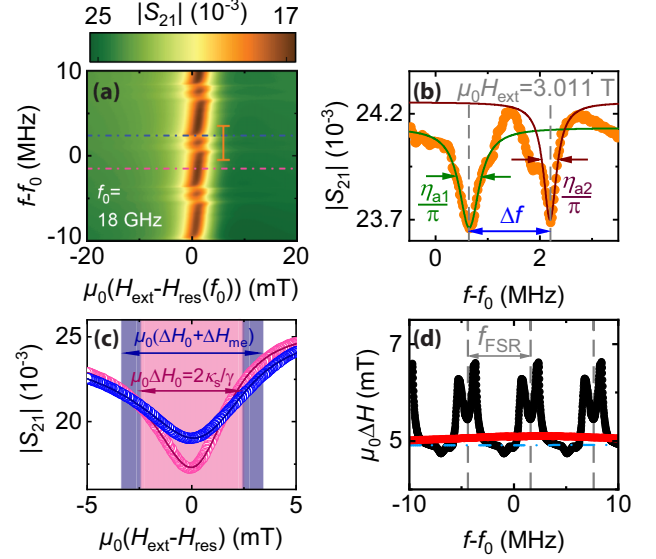


FIG. 2. (a) Microwave transmission magnitude $|S_{21}|$ as a function of $f - f_0$ around $f_0 = 18$ GHz and H_{ext} around $\mu_0 H_{\text{res}}(f_0) = 3.005$ T recorded at $T = 5$ K. (b) $|S_{21}|$ along the orange vertical line in (a). We choose $\mu_0 H_{\text{ext}} = 3.011$ T to analyze the unperturbed linewidth of the elastic modes and obtain the BAW resonator decay rates $\eta_{a1,2}$ by fitting two Lorentzian lines to the data (green and brown lines). The blue arrow indicates the spacing of the double peaks Δf . (c) $|S_{21}|$ for the blue (magenta) horizontal dashed lines in (a), which correspond to the resonant (off-resonant) case of the n th bulk elastic resonance interacting with the FMR. On resonance, we observe a linewidth broadening ΔH_{me} . (d) $\Delta H(f)$ is plotted as a function of f for CoFe deposited on a double-side polished c -plane Al_2O_3 substrate (black data points) and a single-side polished c -plane Al_2O_3 substrate (red data points). The gray dashed lines mark the free spectral range f_{FSR} and the light blue dashed line represents the linear dispersion of ΔH with an offset H_{inh} . In contrast, no features in $\Delta H(f)$ are observed for CoFe deposited on a one-side polished Al_2O_3 substrate, where standing acoustic waves are suppressed by the rough substrate surface. Hence, we can attribute the features observed for the double-side polished substrates to the interaction of magnons with the standing transverse bulk acoustic waves of the host crystal.

CoFe deposited on an Al_2O_3 substrate. We observe the characteristic FMR of the CoFe layer, which shows a distinct, frequency periodic pattern, which we interpret as the signature of the interaction between the magnon mode and the high-overtone BAW mediated by MEC and elastic coupling at the interface to the substrate (cf. Refs. [22,28]). The observed double-peak structure with a frequency periodicity of $f_{\text{FSR}} \approx 6.04$ MHz is in good agreement with the expected $f_{\text{FSR}} \approx 6.05$ MHz from Eq. (1) in Al_2O_3 using the material parameters of CoFe and Al_2O_3 ($d = 30$ nm, $L = 510$ μm , $v_{\text{ft,st}} \approx 6.17$ km/s [41], and $\tilde{v}_t = 3.17$ km/s [47]). The detection of two neighboring phonon resonances with a frequency separation of $\Delta f \approx 1.40$ MHz suggests the presence of two nondegenerate transverse acoustic phonon velocities in the substrate differing by $\Delta v_t \approx 0.5$ m/s. We can resolve this small velocity difference due to low acoustic damping of the acoustic modes at low temperatures. As $d \ll L$, the impact of variations in \tilde{v}_t , d , and θ_m are negligible [see Appendix A 7 and also Fig. 3(c)].

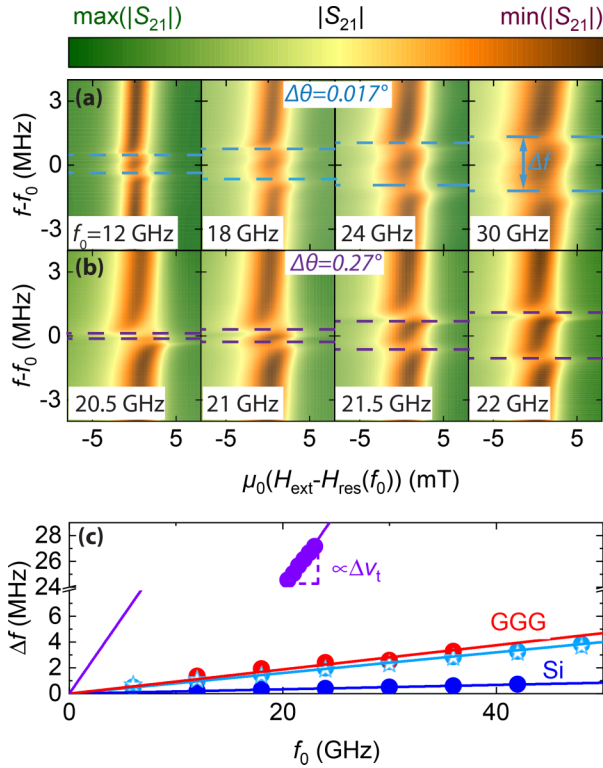


FIG. 3. (a) Microwave transmission magnitude $|S_{21}|$ as a function of frequency f and external magnetic field H_{ext} in narrow frequency ranges around different frequencies f_0 recorded at $T = 5$ K for a CoFe thin film deposited on c -axis Al_2O_3 substrate with a miscut angle $\theta_m^{\text{XRD}} = 0.011^\circ$. (b) A second sample with CoFe deposited on a c -axis Al_2O_3 substrate with a miscut angle of $\theta_m^{\text{XRD}} = 0.27^\circ$. The light blue and purple dashed lines are a guide to the eye indicating that Δf scales linearly with f_0 for both samples. The H_{res} values as well as $\min(|S_{21}|)$ and $\max(|S_{21}|)$ at the respective f_0 are listed in Tables I and II. Note that the frequency spacing of the panels in (a) is 6 GHz, whereas in panel (b) it is 0.5 GHz. (c) The observed frequency splitting Δf for the CoFe thin films deposited on various substrate materials with different crystalline symmetries (light blue and purple for the Al_2O_3 samples in panels (a) and (b), red for GGG, and dark blue for Si) and θ_m . In addition, the panel shows $\Delta f(f)$ for a CoFe/ c -plane Al_2O_3 sample (open star symbols) fabricated from the same wafer as in panel (a) with a thicker CoFe layer ($d = 50$ nm) to demonstrate the negligible impact of the CoFe layer thickness on $\Delta f(f)$. Continuous lines indicate linear fits following Eq. (2) to extract $v_{\text{r}} - v_{\text{st}}$.

Following Ref. [28], we extract the undisturbed linewidth of the elastic modes from a linescan at constant $\mu_0 H_{\text{ext}} = 3.011$ T detuned from the FMR [orange vertical line in Fig. 2(a)] and the FMR linewidth from a fixed-frequency linescan detuned from the acoustic modes [dashed magenta line in Fig. 2(a)]. The respective data are presented in Figs. 2(b) and 2(c). We find the BAW decay rates $\eta_{\text{al},2}/(2\pi) \approx (0.23 \pm 0.02)$ MHz, (0.16 ± 0.01) MHz, and the FMR damping rate $\kappa_s/(2\pi) \approx (69.0 \pm 0.1)$ MHz from the half-width-at-half-maximum linewidth of the elastic resonances and FMR, respectively. The BAW decay rates translate to a BAW decay length of $2\pi\delta_{1,2} = v_t/\eta_{\text{al},2} \approx 2.6$ cm, 3.8 cm $> 2L$ at $f_0 = 18$ GHz supporting the formation of

standing waves in the Al_2O_3 substrate. To quantify the MEC, we calculate the coupling rate g_{MEC} with the model in Ref. [22] (see Appendix B). We obtain the coupling rate $g_{\text{MEC}1,2}/2\pi \simeq 6.0$ MHz at $f_0 = 18$ GHz assuming a magnetoelastic constant of $B = 15.7 \times 10^6$ J/m³ (see Appendix B), a mass density of $\rho = 8110$ kg/m³, and a transverse velocity of $\tilde{v}_t = 3.17$ km/s for CoFe [47].

In this regime, we can understand additional losses visible in the FMR as Purcell enhanced damping due to the coupling to the acoustic resonator [48–50] as shown in Fig. 2(d). Here, we plot the FMR linewidth of CoFe deposited on a double-side polished c -plane Al_2O_3 substrate (black data points). For comparison, we perform the same experiment with a one-side polished crystalline Al_2O_3 substrate. We find an absence of peak features in the magnetic resonance linewidth [see red data points in Fig. 2(d)], indicating that this signature is linked to the formation of standing acoustic waves in the substrate. Obviously, the study of $\Delta H(f)$ provides a very sensitive probe to detect phonon modes in our experiments ($\Delta v_t/v_t = \eta_a/(2\pi f_0) \simeq 10^{-5}$ comparable to Brillouin spectroscopy [51]). In addition, this analysis grants access to the intrinsic magnetization damping mechanisms. Note that the light blue dashed line corresponds to the linewidth evolution captured by the Gilbert damping parameter $\alpha = (2.8 \pm 0.1) \times 10^{-3}$ with an inhomogeneous linewidth of $H_{\text{inh}} = (1.6 \pm 0.3)$ mT (see Appendix A 1).

B. Phononic birefringence in sapphire

Next, we investigate the splitting of the acoustic modes on a broader frequency scale between 12 and 30 GHz [see Fig. 3(a)] for the exemplary case of a 30-nm CoFe thin film deposited on a 510- μm -thick Al_2O_3 substrate with a c -axis miscut angle of $\theta_m^{\text{XRD}} = 0.011^\circ$. The visible frequency splitting of the two MEC features as a function of frequency $\Delta f(f)$ is plotted in Fig. 3(c) (light blue data points). We find that the observed frequency separation Δf of the two standing transverse phonon modes scales linearly with f_0 . This is expected since [cf. Eq. (1)]

$$\Delta f = f_n^{\text{ft}} - f_n^{\text{st}} \approx \frac{v_{\text{ft}} - v_{\text{st}}}{\lambda_n} \quad (2)$$

decreases linearly with f_0 . Here, $\lambda_n = v_t/f_n$ and $v_t \approx v_{\text{ft}}, v_{\text{st}}$. Note that this splitting also manifests itself as two different $f_{\text{FSR},i}$ values for both modes. However, the precision of the latter is insufficient to determine the velocity difference of $\Delta v_t \approx 0.5$ m/s observed here. For sapphire, $v_{\text{ft}} = v_{\text{st}}$ for sound propagation along the c axis [cf. Fig. 1(b)]. Assuming that the presence of two slightly different propagation velocities v_{ft} and v_{st} originates from a slight misalignment between the propagation direction \mathbf{z} and the c axis of the sapphire crystal, we can estimate $\theta_m^{\text{MEC}} \approx 0.017^\circ$ [see Fig. 1(d)]. Here, we neglect the φ dependence. We independently determine the miscut angle from x-ray diffraction (XRD) experiments for this sample to be $\theta_m^{\text{XRD}} = 0.011 \pm 0.002^\circ$ (see Appendix A 4). Note that θ_m^{XRD} determined here corresponds to the global substrate miscut θ_m . Potential local variations originating from the surface morphology can contribute to the determined acoustic linewidth. This local distribution in θ_m might explain the experimentally determined acoustic linewidth $\eta_{\text{al},2}$ at

TABLE III. Miscut angle of the substrates determined via XRD (θ_m^{XRD}) and the calculated θ_m^{MEC} corresponding to the experimentally observed splitting of the MEC features in FMR. We find a good agreement between the resulting θ_m from splitting of the MEC features and XRD experiments.

Substrate	θ_m^{XRD} (deg)	θ_m^{MEC} (deg)
Al ₂ O ₃ (0001) from Fig. 3(a)	0.011	0.017
Al ₂ O ₃ (0001) from Fig. 3(b)	0.27	0.25
Si(001)	0.15	0.17
GGG(111)	0.17	0.21

$f_0 = 18$ GHz discussed above (see Appendix A 5). To test our conjecture that the double peaks originate from nondegenerate modes due to a sample miscut, we perform experiments on a second CoFe thin film on a different *c*-plane Al₂O₃ substrate with a higher miscut angle $\theta_m^{\text{XRD}} = 0.27^\circ$ determined via XRD in Fig. 3(b). Here, we study the splitting of the acoustic modes between 20.5 and 22 GHz and find a much larger scaling of Δf with f_0 , which translates into a periodic splitting of the two MEC features Δf by a full free spectral range $f_{\text{FSR}} = 6.04$ MHz at frequency increments of $\simeq 5$ GHz. Hence, at the frequency range displayed in Fig. 3(b), the two MEC coupling features are already shifted against each other by $\Delta n = 4$ mode numbers as is displayed in Fig. 3(c) (see purple data points). The evolution of this splitting can be translated into a velocity splitting of the two transverse modes of $\Delta v_t \approx 9$ m/s corresponding to $\theta_m^{\text{MEC}} \approx 0.25^\circ$. This miscut angle again matches the θ_m^{XRD} obtained from our XRD (see Table III).

We expect from Eq. (1) that the thickness of the CoFe layer has only a minimal impact on the observed phononic signatures. To test this conjecture, we fabricated a CoFe on *c*-axis Al₂O₃ sample on the same Al₂O₃ wafer as in Fig. 3(a) (to ensure the same macroscopic miscut angle θ_m) using a thicker CoFe layer with thickness $d = 50$ nm and extracted $\Delta f(f)$ for this sample. The resulting $\Delta f(f)$ is plotted as open blue star symbols in Fig. 3(c). We find an almost identical frequency splitting as in the sample presented in Fig. 3(a) irrespective of the thickness of the CoFe layer. This indicates that the splitting of the double-peak features originates from the global miscut angle of the used Al₂O₃ substrate as expected from Eq. (1).

C. Phononic birefringence in different substrate materials

In a last step, we investigate whether these observations are unique to CoFe on hexagonal Al₂O₃. To this end, we deposit CoFe films on cubic GGG and Si substrates. Figure 4 shows the fitted FMR linewidth $\Delta H(f)$ as a function of f . We find that the double-peak features in $\Delta H(f)$ are not unique to hexagonal Al₂O₃ substrates [see Fig. 2(d)] but are also observed for CoFe grown on 380- μm -thick (111)-oriented cubic GGG [Fig. 4(a)] and on 675- μm -thick (100)-oriented cubic Si [Fig. 4(b)]. For all substrate materials, the visible $\Delta f(f)$ of the MEC features is plotted in Fig. 3(c) and the extracted θ_m^{MEC} are in good agreement with the θ_m^{XRD} values determined via XRD, which are listed in Table III.

As expected, the splitting Δf and the free spectral range f_{FSR} of the overtone resonances differ for the various substrates, as the absolute values of v_{st} and v_{ft} are mate-

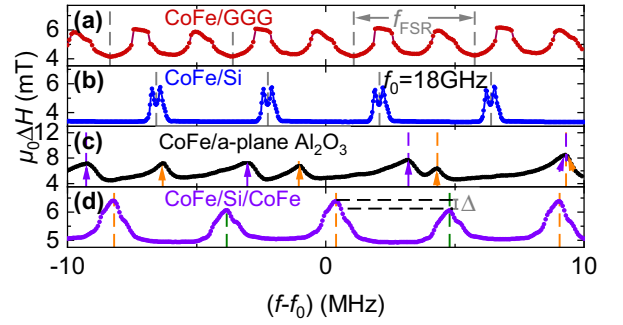


FIG. 4. FMR linewidth $\Delta H(f)$ recorded at $T = 5$ K as function of f around $f_0 = 18$ GHz for CoFe deposited on various substrate materials. Pronounced MEC peaks are observed on (a) a 380- μm -thick GGG (111) substrate ($\theta_m^{\text{XRD}} = 0.17^\circ$), (b) a 675- μm -thick Si (100) substrate ($\theta_m^{\text{XRD}} = 0.15^\circ$), (c) a 500- μm -thick *a*-plane Al₂O₃, and (d) CoFe deposited symmetrically on both sides of a 675- μm -thick Si (100) substrate. Gray dashed lines indicate the f_{FSR} , whereas orange and purple arrows in panel (c) indicate the BAW resonance modes of the two strongly degenerate phonon modes for *a*-plane Al₂O₃ and olive dashed lines in panel (d) indicate even or odd acoustic resonance modes exhibiting an alternating ΔH .

rial specific. Note that acoustic impedance matching is of minor importance here, as the CoFe film thickness is small compared to the acoustic wavelength even at 50 GHz (see Appendix A 7). In addition, the magnitude of both the off- and on-resonant FMR linewidth is comparable for all substrates. This suggests (i) that the magnetization damping and thus the magnetic properties of the CoFe film are consistent for the various substrates, (ii) that the acoustic damping as well as the thicknesses of the substrates are similar, and (iii) that the underlying excitation mechanism is governed by the material parameters of CoFe [30,47].

So far, we have only discussed experiments for phonons injected along crystallographic directions, where the two transverse phonon velocities are expected to be degenerate. Alternatively, we can select a crystallographic direction along which the two transverse modes are expected to be non-degenerate such as, for example, the *a* direction of Al₂O₃. In Fig. 4(c), we plot the FMR linewidth $\Delta H(f)$ at 5 K for CoFe grown on *a*-plane sapphire [(11 $\bar{2}$ 0) orientation] for $f_0 = 18$ GHz. Two periodic peak features [see orange and purple arrows in Fig. 3(c)] with visibly different free spectral ranges $f_{\text{FSR},1} \simeq 5.36$ MHz and $f_{\text{FSR},2} \simeq 6.24$ MHz are apparent. Assuming a substrate layer thickness of $L = 500$ μm , these $f_{\text{FSR},i}$ values translate to $v_{\text{ft}} \approx 6.24$ km/s and $v_{\text{st}} \approx 5.36$ km/s. These values correspond to the theoretically calculated values for v_{ft} and v_{st} in Fig. 1(b). This result underlines that the shear wave velocity difference which is key for phononic birefringence indeed can be controlled by selecting a suitable substrate cut and propagation length for the respective experiment. Finally, in Fig. 4(d) we study ΔH for a symmetric CoFe/Si/CoFe sample using a substrate from the same wafer as in Fig. 4(b). While the free spectral range is nearly identical for the two samples, the FMR linewidth ΔH is significantly enhanced for the CoFe/Si/CoFe stack. We attribute this to additional effective acoustic damping induced by the second CoFe layer. In addition, we find that the acoustic modes show

an alternating amplitude of ΔH . In analogy to the results presented in Ref. [22], we attribute this signature to an alternating coupling strength originating from the phonons of different chirality for even and odd n . Indeed, we expect this behavior for our Si substrate, as the difference between v_{st} and v_{ft} is small, resulting in a mode overlap of both orthogonal phonon polarizations.

IV. CONCLUSION

We report the magnetoelastic coupling between the ferromagnetic resonance mode in a ferromagnetic metal and the transverse acoustic phonon modes of high-overtone bulk acoustic resonators in the Purcell enhanced regime. Using thin polycrystalline ferromagnetic CoFe films to drive the acoustic excitations, we explore Al_2O_3 , Si, and GGG as phononic host materials, where Si and Al_2O_3 provide a perspective to enter the quantum regime. As the chirality of the ferromagnetic resonance modes can excite circularly polarized elastic shear waves in the substrates which carry angular momentum, this excitation scheme is ideal for the investigation of phononic angular momentum transport. The use of CoFe demonstrated here can be extended to a multitude of substrates with diverse phononic properties and hereby establish a platform for future experiments on phononic birefringence [52,53] and long-range angular momentum transport with phonons. Even experiments combining phonon caustics [54] and angular momentum transport could come in reach.

ACKNOWLEDGMENTS

We acknowledge financial support by the Deutsche Forschungsgemeinschaft (DFG, German Research Foundation) via Germany's Excellence Strategy EXC-2111-390814868, SFB 1432 (Project ID 425217212) and TRR 360 (Project ID 492547816). F.E., V.A.S.V.B., M.C., and S.V.K. thank Sanchar Sharma for useful discussions and acknowledge funding from the Bundesministerium für Bildung und Forschung (BMBF, Grant No. 16KIS1590K) and from the Deutsche Forschungsgemeinschaft (DFG, German Research Foundation) through (Project ID 429529648–TRR 306) QuCoLiMa (“Quantum Cooperativity of Light and Matter”) and rtg 1995. This research is part of the Munich Quantum Valley, which is supported by the Bavarian state government with funds from the Hightech Agenda Bayern Plus. V.A.S.V.B. acknowledges funding from the Contrat Triennal 2021–2023 Strasbourg Capitale Européenne. Furthermore, we want to thank Kedar Honasoge for his help with scanning electron microscopy.

APPENDIX A: ADDITIONAL EXPERIMENTAL DATA

1. Parameters describing the magnetization dynamics in CoFe

The parameters determining the magnetization dynamics are important to describe the magnetic system. We have derived these parameters from the results of broadband ferromagnetic resonance (FMR) experiments. We fit the raw data as described in Ref. [44] and extract the FMR resonance frequency and linewidth in a frequency spacing in the

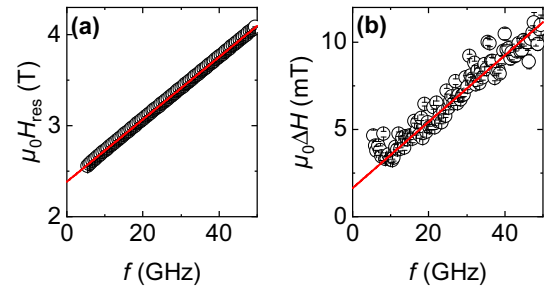


FIG. 5. (a) Resonance field $\mu_0 H_{\text{res}}(f)$ of the $\text{Al}_2\text{O}_3/\text{CoFe}$ sample at $T = 5$ K plotted versus frequency. The line shows a fit of the data to Eq. (A1) and is used to extract the g factor and the effective magnetization M_{eff} . (b) Resonance linewidth $\mu_0 \Delta H(f)$ of the $\text{Al}_2\text{O}_3/\text{CoFe}$ sample at $T = 5$ K together with a fit to Eq. (A2) (red line) used to extract H_{inh} and α .

gigahertz range, where the contributions from the elastic resonances average out. Figures 5(a) and 5(b) show exemplary data for the resonance field $H_{\text{res}}(f)$ and linewidth $\Delta H(f)$ of the $\text{Al}_2\text{O}_3/\text{CoFe}$ sample at $T = 5$ K. To characterize the effective magnetization M_{eff} and the g factor of the magnetic system, the frequency dependence of the resonance field $H_{\text{res}}(f)$ is fitted using

$$\mu_0 H_{\text{res}} = \mu_0 M_{\text{eff}} + \frac{h}{g\mu_B} f, \quad (\text{A1})$$

where h is the Planck constant and μ_B is the Bohr magneton. We extract a g factor of $g = 2.079 \pm 0.001$ and an effective magnetization $\mu_0 M_{\text{eff}} = (2.381 \pm 0.004)$ T at $T = 5$ K corresponding to the expected values for CoFe of this material composition, $\text{Co}_{25}\text{Fe}_{75}$ [44].

The frequency dependence of the FMR linewidth $\mu_0 \Delta H(f)$ is fitted with the linear model following Eq. (A2) to extract the Gilbert damping parameter α , which is proportional to the slope of the $\mu_0 \Delta H(f)$ dependence, and the inhomogeneous broadening $\mu_0 H_{\text{inh}}$ as its y -axis intercept [44]:

$$\mu_0 \Delta H(f) = \mu_0 H_{\text{inh}} + 2 \frac{h\alpha}{g\mu_B} f. \quad (\text{A2})$$

We extract an inhomogeneous line broadening of $\mu_0 H_{\text{inh}} = (1.6 \pm 0.2)$ mT and a Gilbert damping $\alpha = (2.8 \pm 0.1) \times 10^{-3}$ at $T = 5$ K, which is in good agreement with the room-temperature values reported in Ref. [44].

2. Anisotropy of the CoFe thin films

Anisotropy fields present in magnetic materials can affect the details of the dynamic response and, in particular, modify the dynamic precession of the magnetic moment. To quantify potential anisotropy fields, we extract M_{eff} from broadband FMR experiments (see Fig. 5) and compare this value with the saturation magnetization M_s recorded via in-plane superconducting quantum interference device (SQUID) magnetometry. We find $M_{\text{eff}} \approx M_s$ as shown in Fig. 6, corresponding to a negligible magnetic anisotropy besides the shape anisotropy in our samples. This suggests that we can neglect pronounced anisotropy contributions beyond the shape anisotropy, in particular induced by the texturing in our thin-film samples.

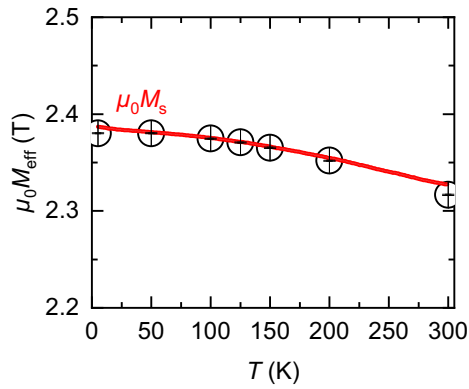


FIG. 6. Temperature dependence of the effective magnetization M_{eff} (open circles) extracted from broadband FMR experiments plotted together with the saturation magnetization M_s (red solid line), which has been determined via in-plane SQUID magnetometry measurements in an external magnetic field of $H_{\text{ext}} = 50$ mT.

3. Chiral character of the pumped phonon modes

Within the field of phonon-mediated spintronics, it has been theoretically predicted that the efficiency of the excitation of a ferromagnetic resonance mode depends on the magnetoelastic coupling and on the chirality of the phonons [29,30]. In the experimental works of An *et al.* [22,23], chiral phonons have been indirectly detected via FMR experiments in symmetric YIG/GGG/YIG heterostructures, where the coupling strength between the FMR modes of the top and bottom layers depends on the index n of the phonon mode. Experimentally, this manifests in an alternating FMR amplitude (when the FMR is resonant with a phonon mode of the bulk acoustic resonator) depending on whether the acoustic overtone number is even or odd [22]. In their experiment, the ferromagnetic resonance amplitude, when interacting with an acoustic resonance in the GGG host crystal, exhibited different magnitudes in the energy absorption, which the authors attributed to the superposition of the microwave driving field and the circularly polarized elastic excitation acting on one of the films. In detail, this results in an enhanced or suppressed overall excitation field depending whether even or odd modes are at play, and manifests as an alternating signature in the recorded FMR absorption. As these features were only detected in symmetric YIG/GGG/YIG samples and have been absent in asymmetric YIG/GGG bilayers, the detection of an altered MEC for even or odd acoustic modes has been identified as an indirect evidence for the pumping of chiral phonons in Ref. [22]. Having this experiment in mind, we fabricated symmetric CoFe/Si/CoFe heterostructures to investigate the coupling of distant magnetic layers via chiral phonons in our experiments. The resulting magnetization dynamics of the bottom CoFe layer at $T = 5$ K around $f_0 = 18$ GHz is plotted in Fig. 7. Compared to the data for the asymmetric layer layout (CoFe/Si) presented in Figs. 7(a) and 7(b), Figs. 7(c) and 7(d) show the data for a symmetric CoFe/Si/CoFe layer stack, which exhibits an alternating behavior in the FMR amplitude and the FMR magnetic field linewidth. This evolution is similar to the observations reported by An *et al.* for the YIG/GGG and YIG/GGG/YIG system [22] and hence we understand

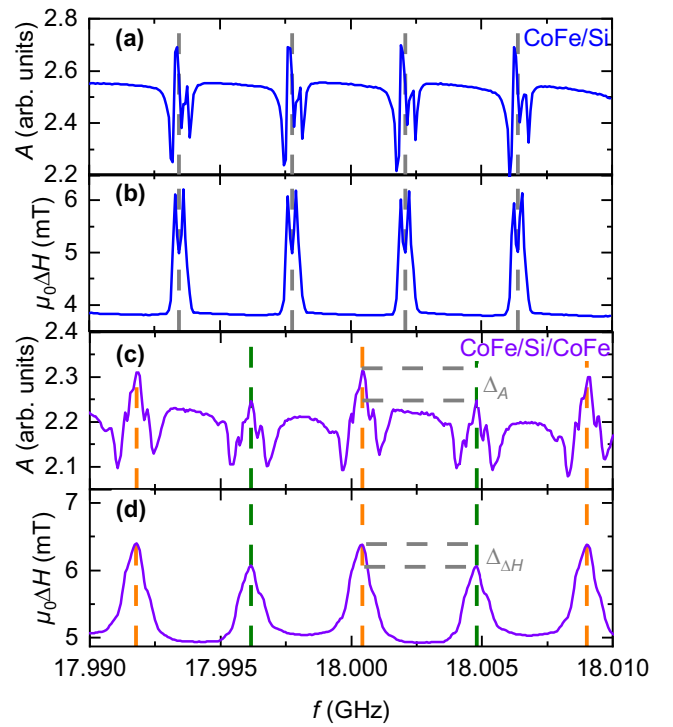


FIG. 7. [(a), (c)] FMR amplitude A , a measure of the power absorption of the system, and [(b), (d)] FMR linewidth modulation $\Delta H(f)$ plotted for frequencies around $f_0 = 18$ GHz at $T = 5$ K for [(a), (b)] CoFe deposited on one side of a (100)-oriented Si substrate and [(c), (d)] CoFe deposited on both sides of a (100)-oriented Si substrate ($L = 675$ μm). For the symmetric CoFe/Si/CoFe sample, we clearly observe different magnitudes in both FMR amplitude and linewidth for the sample magnetization coupling to even (orange dashed lines) or odd (olive dashed lines) acoustic modes due to the constructive or destructive interference of the magnetization dynamics in the two CoFe layers mediated by the exchange of chiral phonons over the substrate. These features are absent in the asymmetric CoFe/Si sample in panels (a) and (b) (vertical gray dashed lines indicate the acoustic resonances).

this as an indication of circular polarized phonon transport in our symmetric CoFe/Si/CoFe structures. Note that for Fig. 7, we deliberately chose silicon as the substrate material, for which we find a mode overlap of the two transverse shear waves. We find a different modulation of both FMR amplitude and linewidth for frequencies, where the magnetization in the bottom CoFe layer is coupled to elastic resonances in the Si substrate with even (orange dashed lines) and odd (olive dashed lines) mode numbers. The FMR amplitude in Fig. 7(a) is a measure for the power absorption of the sample in analogy to the experiments in Ref. [22]. However, we also find a different modulation in the FMR linewidth ΔH in Fig. 7(b) induced by the different coupling strengths between the two magnetic layers. In analogy to the results presented in Ref. [22], we identify the alternating amplitude in Figs. 7(c) and 7(d) as the signature for the presence of chiral phonons in our experiments. In addition, the data in Fig. 7(a) show pronounced dips in FMR response. We attribute this to magnon-phonon coupling present in our experiments. In particular, we are in a regime which can be interpreted as analog to the Purcell

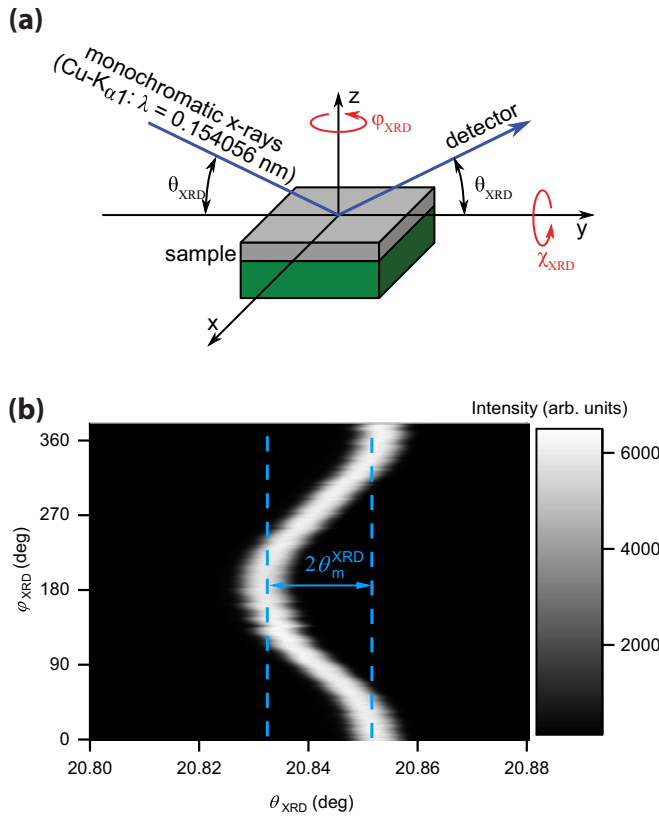


FIG. 8. (a) Measurement geometry for the XRD experiments using an x-ray diffractometer with Cu $K\alpha_1$ radiation. Prior to the measurements, the azimuthal rotation axis is aligned parallel to the surface normal of the sample. To determine the miscut angle, rocking curves around the Al_2O_3 (0006) substrate reflection at different azimuthal angles have been performed. (b) X-ray intensity of the (0006) reflection of the Al_2O_3 substrate for the CoFe on a c -axis Al_2O_3 sample from Fig. 3(a) as function of φ_{XRD} and θ_{XRD} . The variation of the maximum of the (0006) reflection is assigned to the imperfect alignment of the sample surface with respect to the crystallographic axes of Al_2O_3 . Specifically, we can determine $\theta_{\text{m}}^{\text{XRD}} = (0.011 \pm 0.002)^\circ$ (see blue dashed lines), which is in good agreement with $\theta_{\text{m}}^{\text{MEC}} = 0.017^\circ$ determined via our FMR experiments.

enhanced regime for the FMR, which can result in those signatures [50].

4. Determination of the substrate miscut angle by x-ray diffraction

Due to imperfections in the cutting and polishing process of the substrates the surface normal of the single crystalline substrates is typically not perfectly aligned parallel to the specified crystallographic axis but may slightly deviate from it by a finite angle, which we call the miscut angle θ_{m} . To quantify the miscut angle for the specific samples, we performed high-resolution x-ray diffraction experiments on our samples presented in the main text. Specifically for the CoFe/ Al_2O_3 samples, we studied the change of the angle of incidence, θ_{XRD} , of the (0006) reflection of the Al_2O_3 substrate originating from a finite miscut denoted as θ_{m} as a function of the angle φ_{XRD} [see Fig. 8(a) for the measurement geometry].

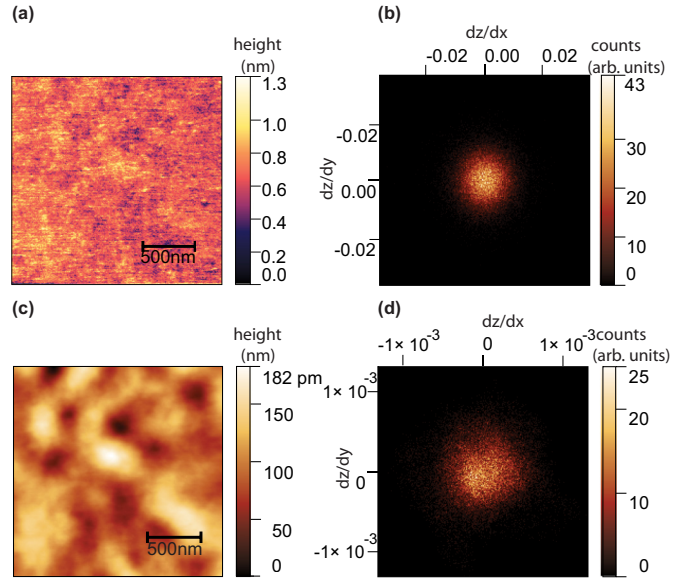


FIG. 9. (a) Atomic force microscopy (AFM) surface scans of a $4 \mu\text{m}^2$ area for a bare c -axis-oriented Al_2O_3 substrate. No large variations in sample height are observed on this lateral length scale. The observed maximum height variation between highest and lowest points in this scan area is approximately 1.3 nm. (b) Slope distribution map of the AFM scan shown in panel (a). (c) AFM surface scan from panel (a) after averaging the height profile with a characteristic length scale of $\simeq 120$ nm. (d) Slope distribution map of the filtered AFM scan shown in panel (c).

Before the measurement we align the sample in such a way that the azimuthal rotation axis is parallel to the surface normal of the substrate using the total reflection in grazing incidence diffraction geometry. Then we record rocking curves around the Al_2O_3 (0006) reflection for different azimuthal angles. The result is plotted in Fig. 8(b). The observed $\theta_{\text{m}}^{\text{XRD}}$ of $(0.011 \pm 0.002)^\circ$ is in good agreement with the calculated value $\theta_{\text{m}}^{\text{MEC}} = 0.017^\circ$ for this sample determined via the frequency splitting of the two transverse modes and the related velocity splitting following the Christoffel equation. Using this experimental method, we determine $\theta_{\text{m}}^{\text{XRD}}$ for all of the samples from corresponding substrate reflections in this study. The results are listed in Table III.

5. Dichotomy between local and global substrate miscut

Besides the global substrate miscut, local variations in miscut angle θ_{m} of the substrate (on the length scale of the phononic wavelength) can occur, which can affect the (local) velocities of the two phonon branches and cause a distribution of the phonon propagation directions in the substrate. The effects of the propagation direction distribution in combination with the boundary conditions will cause a distribution of the acoustic resonance frequencies. We attempt to quantify the local distribution of θ_{m} using atomic force microscopy. Figure 9(a) shows a representative surface morphology of the surface of the c -axis-oriented Al_2O_3 crystal used for this study for which we find an RMS roughness of 1.3 nm. From these data, we can compute the slope distribution [see Fig. 9(b)]; however, this distribution includes noise and potentially

surface height modulations on short length scales. For a better estimate, we also present the slope distribution after averaging the height profile over a lateral characteristic length scale of ≈ 120 nm, which corresponds to the acoustic wavelength of transverse phonons in Al_2O_3 at 50 GHz [see Fig. 9(c) for the result of the filtered AFM scan]. This more narrow distribution should give an indication of the variation of θ_m , which we estimate to $\pm 0.006^\circ$ [see Fig. 9(d)]. To evaluate the impact of $\Delta\theta_m$ in our experiments, we estimate the acoustic linewidth broadening induced by a distribution of θ_m from Eq. (1). Here, we define the induced broadening Δf_L by $\Delta\theta_m$ due to a change in effective sample length $\Delta L = L / \cos \Delta\theta_m - L$ as

$$\Delta f_L = \frac{\partial f_n}{\partial L} \Delta L. \quad (\text{A3})$$

Likewise, following Fig. 1(d), $\Delta\theta_m$ modifies the group velocities of fast and slow transverse modes by $\Delta v_{\text{ft,st}}$. We account for this contribution of the transverse velocity distribution on Δf via

$$\Delta f_{v_{\text{ft,st}}} = \frac{\partial f_n}{\partial v_{\text{ft,st}}} \Delta v_{\text{ft,st}}. \quad (\text{A4})$$

We insert the material parameters for CoFe ($d = 30$ nm, $\tilde{v}_t = 3.17$ km/s) and Al_2O_3 ($L = 510$ μm and $v_t = 6.17$ km/s and $\Delta v_{\text{ft,st}}(\Delta\theta_m) = 0.08$ m/s [see Fig. 1(d)]) and using a BAW mode number of $n = 3000$ for frequencies around 18 GHz and obtain $\Delta f_L \simeq 50$ Hz and $\Delta f_{v_{\text{ft,st}}} \simeq 100$ kHz. Notably, the magnitude of $\Delta f_{v_{\text{ft,st}}}$ is comparable to the fitted η_a in the main text. Hence, we infer that the morphology of the substrate surface plays a crucial role for the damping of the phononic modes.

For comparison, we also analyze the high-resolution XRD data presented in Fig. 8 with respect to the distribution of θ_m . From this XRD experiment, we find that the full width at half maximum $\Delta\theta_{\text{XRD}}$ in θ_{XRD} of the crystalline (0006) reflection of c-axis Al_2O_3 is $\Delta\theta_{\text{XRD}} \approx 0.005^\circ$ and thus agrees with the estimation above. Note that the width of this rocking curve indicates the mosaicity, i.e., the misorientation of the individual crystallites in the substrate. As expected for a bulk commercial Al_2O_3 crystal, we find that the mosaicity is small compared to θ_m in our experiments.

6. Impact of crystalline texturing and grains on the formation of acoustic standing waves

The XRD scans on our CoFe thin film in Fig. 10 reveal a CoFe (110)-reflection induced by the (111)-textured Pt seed layer.

Regarding the validity of Eq. (1) in the presence of crystalline grains and a lateral nonuniformity of the velocity of the transverse modes in the CoFe layer \tilde{v}_t , we note that the contribution of the CoFe layer to f_{FSR} is very minor due to the low layer thickness of the FM film. Plugging $v_t = 6.17$ km/s, $L = 510$ μm , $\tilde{v}_t = 3.17$ km/s, and $d = 30$ nm into Eq. (1), we obtain $f_{\text{FSR}} \approx 6.04833$ MHz. If we assume that the CoFe layer has regions, where \tilde{v}_t differs from this value by $\pm 10\%$, we obtain the free spectral ranges $f_{\text{FSR}\pm 10\%} \approx (6.04825/6.04839)$ MHz. At a frequency of $f_0 = 18$ GHz ($n \simeq 3000$), this would translate into a frequency splitting of $\Delta f = 0.4$ MHz, which is still below the detected

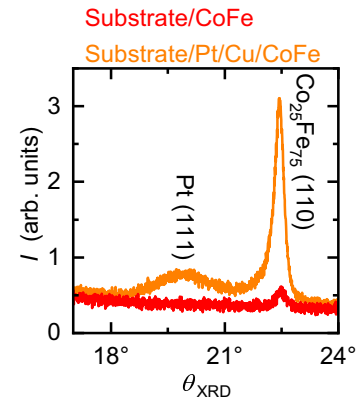


FIG. 10. XRD scans of two different $d_{\text{CoFe}} = 30$ nm CoFe multilayer samples revealing CoFe as well as Pt(111) reflections for the multilayer sample with a Pt seed layer.

$\Delta f \approx 1.4$ MHz for this frequency. Also note that in reality, we would expect a distribution of velocities around \tilde{v}_t rather than two discrete values giving rise to the twofold MEC feature splitting.

Finally, in Fig. 11, we show an exemplary scanning electron microscope (SEM) image for the CoFe layer grown on a c-axis Al_2O_3 substrate to obtain information about the typical grain size in our CoFe layer. A random distribution of small grains with characteristic dimensions of approximately 10–30 nm is observed. Consequently, we do not expect the grain formation in our CoFe thin films to affect the strain pattern and magnetoelastic coupling in our thin films.

7. Role of acoustic impedance matching in our experiments

In our experiments, the acoustic impedance matching between sample and FM thin films does not affect the linearity in the splitting of the MEC features as will be discussed in the following. Using Eq. (38) in Ref. [30], the resonance condition for standing waves is given by

$$\sin(\tilde{k}_t d) \cos(k_t L) + \frac{Z}{\tilde{Z}} \cos(\tilde{k}_t d) \sin(k_t L) = 0. \quad (\text{A5})$$

Here, \tilde{k}_t and k_t are the phonon wave numbers of the ferromagnetic thin film and the respective substrate, whereas \tilde{Z} and Z represent the acoustic impedance of the FM thin film and

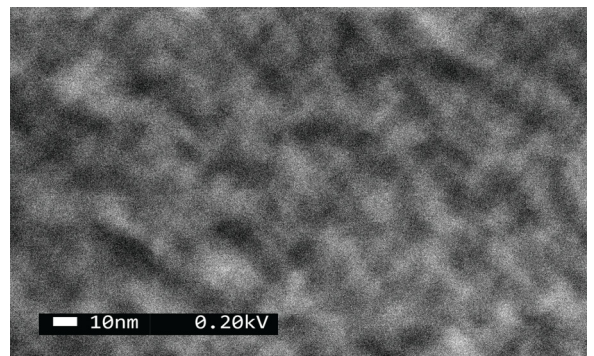


FIG. 11. Scanning electron microscope scan for the CoFe layer grown on a c-axis Al_2O_3 substrate. A random distribution of small circular grains is visible.

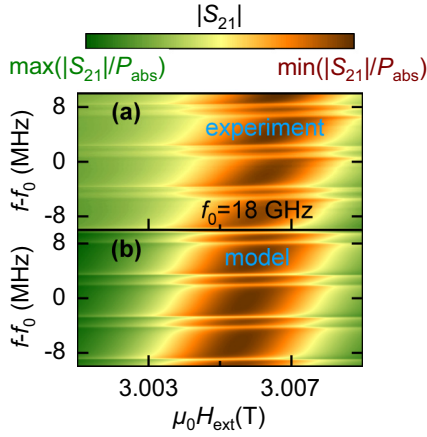


FIG. 12. (a) $|S_{21}|$ recorded at $T = 5$ K and plotted as a function of f and H_{ext} in the range of $\mu_0 H_{\text{res}} = 3.005$ T corresponding to $f_0 = 18$ GHz. (b) Simulation of P_{abs} plotted as a function of f and H_{ext} in the range of H_{res} for $f_0 = 18$ GHz using the parameters listed above. A good agreement between experiment and theory is observed. The plotted power absorption range is (a) from $\min(|S_{21}|) = 0.016$ to $\max(|S_{21}|) = 0.025$ and (b) from $\min(P_{\text{abs}}) = 1.0 \times 10^{-4}$ to $\max(P_{\text{abs}}) = 4.9 \times 10^{-4}$.

substrate. Assuming a good acoustic impedance matching between substrate and FM ($Z \approx \tilde{Z}$), this condition is fulfilled for frequencies given by Eq. (1). Note that the acoustic impedance matching between CoFe and Al_2O_3 as well as between CoFe and GGG is excellent ($Z_{\text{Al}_2\text{O}_3}/\tilde{Z} \simeq 0.93$ and $Z_{\text{GGG}}/\tilde{Z} \simeq 0.97$ using the material parameters for CoFe and Al_2O_3 from the main text, and that of GGG from Ref. [30]). Hence, Eq. (1) may be used. We further note that, with these substrate materials, the acoustic impedance matching is even superior to that of YIG grown on GGG ($Z_{\text{GGG}}/\tilde{Z}_{\text{YIG}} \simeq 1.27$ [30]).

For the case of Si, we use the material parameters from Ref. [42] and obtain an acoustic impedance matching of $Z_{\text{Si}}/\tilde{Z} \simeq 0.55$. However, due to the low layer thickness of the FM layer of $d = 30$ nm, we can assume $\tilde{k}_t d \approx 0$ for frequencies in the intermediate gigahertz range and arrive at the simplified form of Eq. (A5):

$$\frac{Z}{\tilde{Z}} \sin(k_t L) = 0. \quad (\text{A6})$$

Obviously, this relation is fulfilled for $f_{n,i} = n v_t / (2L)$ irrespective of the impedance matching. Hence, due to the low layer thickness of the FM layer, any nonlinear higher-order f terms in the solution to $f_{n,\text{ft}}$ and $f_{n,\text{st}}$ and consequently to Δf do not play a role in our experiments, but are expected to manifest at high frequencies and for samples with a larger d .

APPENDIX B: THEORETICAL MODELING

To model the MEC coupling in Fig. 2(a), we use the formalism derived in Ref. [30]. In detail, we calculate the modified Polder susceptibility $\hat{\chi}_{\text{tot}}$ in the presence of MEC coupling. We plot the experimentally observed $|S_{21}|$ in Fig. 12(a) together with the simulated spectrum of the absorbed power P_{abs} given by Eq. (36) in Ref. [30] in Fig. 12(b) as a function of external field and frequency around $f_0 = 18$ GHz. For our simulation, we use for the

magnetization dynamics parameters the values extracted via broadband ferromagnetic resonance spectroscopy (BBFMR) in Appendix A 1 with $M_s = M_{\text{eff}} = 1.91083 \times 10^6$ A/m, $\alpha = 2.8 \times 10^{-3}$, $\mu_0 H_{\text{inh}} = 1.6$ mT, and $\gamma = g \mu_B / \hbar = 29.13 \times 10^9 \times 2\pi$ s $^{-1}$. For the elastic properties of sapphire and CoFe (denoted with a tilde), we use two transverse phonon velocities in sapphire, $v_{\text{st}} = 6170$ m/s [41], $v_{\text{ft}} = v_{\text{st}} + \Delta v_t$ with $\Delta v_t = 0.5$ m/s, and for CoFe $\tilde{v}_t = 3170$ m/s [47]. Furthermore, we assume the mass densities $\rho_t = 3970$ kg/m 3 (manufacturer's specification) and $\tilde{\rho}_t = 8110$ kg/m 3 [47]. For the elastic damping parameters of the two elastic waves in sapphire and CoFe, we use $\eta_{a1}/(2\pi) = 0.23$ MHz and $\eta_{a2}/(2\pi) = 0.16$ MHz determined from the data presented in the main text. Due to the low layer thickness of the CoFe layer, the elastic damping of the CoFe layer $\tilde{\eta}_a$ can be neglected. Furthermore, we use the geometric properties $L = 510$ μm and $d = 30$ nm as well as $h_{\parallel} = h_{\perp} = 1$ for the parallel and perpendicular driving field components of the coplanar waveguide. Finally, for the magnetoelastic constant B in polycrystalline thin films, we use [55]

$$B = \frac{3}{2} \frac{E}{1 + \nu} \lambda_s, \quad (\text{B1})$$

where E is the Young modulus, ν is the Poisson ratio, and λ_s is the saturation magnetostriction. We insert $E = 220$ GPa [56], $\nu = 0.29$ (sputtering target manufacturer's specification), and $\lambda_s = 0.25 \lambda_s^{\text{Co}} + 0.75 \lambda_s^{\text{Fe}} \approx 6.1 \times 10^{-5}$ [55] in Eq. (B1) and obtain $B = 15.7 \times 10^6$ J/m 3 .

Using these parameters, we observe in Fig. 12 a good agreement between the simulation and the experimental data. We observe a slight frequency shift between theory and experiments due to uncertainties in the thickness L and velocity v_t of the sapphire layer. From Fig. 12, we verify that our assumed material parameters are valid. However, Ref. [30] does not provide an analytical expression of the effective magnetoelastic coupling strength $g_{\text{eff}}(f)$.

Hence, to determine the coupling $g_{\text{eff}}(f)$, we use [22,28]

$$g_{\text{eff}}(f)/(2\pi) = \frac{1}{2\pi} B \sqrt{\frac{2g\mu_B}{hfM_s\tilde{\rho}_t d L}} \left[1 - \cos\left(2\pi f \frac{d}{\tilde{v}_t}\right) \right]. \quad (\text{B2})$$

Using $M_s = M_{\text{eff}}$, $L = 510$ μm , and $d = 30$ nm, the transverse velocity $\tilde{v}_{\text{st}} = 3170$ m/s and $\tilde{\rho}_t = 8110$ kg/m 3 for the volume density in CoFe [47] as well as $B = 15.7 \times 10^6$ J/m 3 , we obtain $g_{\text{eff}}(f_0)/(2\pi) \approx 6.0$ MHz at $f_0 = 18$ GHz.

To prove the validity of this approach, we apply the same formalism as in Ref. [22] and describe our systems as two uncoupled elastic wave modes, each individually coupled to the magnetic Kittel mode. The set of differential equations describing such a model is

$$\begin{aligned} (f - f_m + ik_s/(2\pi))m^x &= g_1 u_n^x/(4\pi) + \zeta h^x, \\ (f - f_m + ik_s/(2\pi))m^y &= g_2 u_n^y/(4\pi) + \zeta h^y, \\ (f - f_n^x + i\eta_{a1}/(2\pi))u_n^x &= g_1 m^x/(4\pi), \\ (f - f_n^y + i\eta_{a2}/(2\pi))u_n^y &= g_2 m^y/(4\pi). \end{aligned} \quad (\text{B3})$$

Here, f_m is the magnetic resonance frequency determined by solving Eq. (A1) for f and the $f_{n,1,2}$ are the resonance frequencies of the elastic standing waves using Eq. (1) with

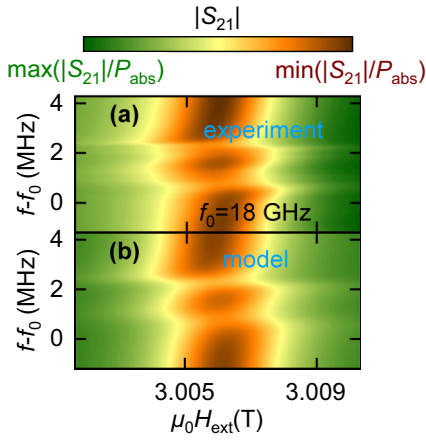


FIG. 13. (a) $|S_{21}|$ recorded at $T = 5$ K and plotted as a function of f and H_{ext} in the range of H_{res} for $f_0 = 18$ GHz corresponding to the $n = 2918$ th BAW resonance mode number ($f_0 \approx f_{2918}^y$). (b) Simulation of P_{abs} obtained by solving Eq. (B3) by $m^x + m^y$ and plotted as a function of f and H_{ext} in the range of H_{res} for $f_0 = 18$ GHz using the parameters listed above. A good agreement between experiment and theory is observed. The plotted power absorption range is (a) from $\min(|S_{21}|) = 0.016$ to $\max(|S_{21}|) = 0.025$ and (b) from $\min(P_{\text{abs}}) = 0.24 \times 10^6$ to $\max(P_{\text{abs}}) = 2.52 \times 10^6$.

v_{ft} and v_{st} . The variables m^x and m^y are the two linearly polarized magnetization amplitudes and likewise the u_n^x and u_n^y are the linearly polarized elastic wave amplitudes propagating at slightly different propagation velocities and hence being in resonance at the frequencies f_n^x and f_n^y . Note that we can assume that m_x is coupled exclusively to f_x and m_y solely to f_y , as we are free to define the x - y coordinate system of the FMR with respect to the polarization of the acoustic modes. The parameter ζ describes the inductive coupling to the antenna and h^x and h^y are the driving field of the coplanar waveguide. The power absorption of this system is given by $P_{\text{abs}} = \zeta (h^x \text{Im}(m^x) + h^y \text{Im}(m^y))$. In Fig. 13, we plot P_{abs} using the elastic and magnetic loss rates $\eta_{a1}/(2\pi) = 0.23$ MHz, $\eta_{a2}/(2\pi) = 0.16$ MHz, and $\kappa_s/(2\pi) = 69.0$ MHz as for Fig. 3, an effective coupling strength of $g_1/(2\pi) = g_2/(2\pi) = 6.0$ MHz, $\zeta = 1$ MHz, and $h^x = h^y = 1$. We again observe in Fig. 13 a good agreement between theory model and the experimental data, demonstrating that the magnitude of our assumed coupling is in agreement with theoretical predictions.

APPENDIX C: MODELING OF THE VELOCITY SPLITTING OF THE TRANSVERSE MODES

In the main text, we have used the Christoffel PYTHON tool from Ref. [40] to calculate the dispersion of the transverse modes and thus v_{ft} and v_{st} as functions of the phonon propagation direction. Here, we derive the exact analytical expression for the transverse velocity splitting as a function of the relative propagation direction with respect to a selected crystallographic axis given by the angle θ .

1. Substrate with hexagonal crystallographic structure

We start by deriving the dispersion relation of the acoustic phonons and their respective group velocities in the sapphire layer taking into account the relative directions between the c axis and the phonon propagation. The components of the stress tensor of the sapphire layer can be written as [57]

$$\begin{aligned}\sigma_{x,x} &= c_{11}\varepsilon_{x,x} + c_{12}\varepsilon_{y,y} + 2c_{14}\varepsilon_{y,z} + c_{13}\varepsilon_{z,z}, \\ \sigma_{y,y} &= c_{12}\varepsilon_{x,x} + c_{11}\varepsilon_{y,y} - 2c_{14}\varepsilon_{y,z} + c_{13}\varepsilon_{z,z}, \\ \sigma_{z,z} &= c_{13}\varepsilon_{x,x} + c_{13}\varepsilon_{y,y} + c_{33}\varepsilon_{z,z}, \\ \sigma_{y,z} &= \sigma_{z,y} = c_{14}\varepsilon_{x,x} - c_{14}\varepsilon_{y,y} + 2c_{44}\varepsilon_{y,z}, \\ \sigma_{x,z} &= \sigma_{z,x} = 2c_{14}\varepsilon_{x,y} + 2c_{44}\varepsilon_{x,z}, \\ \sigma_{x,y} &= \sigma_{y,x} = (c_{11} - c_{12})\varepsilon_{x,y} + 2c_{14}\varepsilon_{x,z},\end{aligned}\quad (\text{C1})$$

where c_{pq} represents the components of the stiffness tensor in Voigt notation, and $\varepsilon_{i,j}$ is the strain tensor. We reshape the strain tensor taking into account the deflection of the c axis by introducing an auxiliary Cartesian coordinate system $\{x', y', z'\}$. The transformation of the strain tensor into the $x'y'z'$ system is given by

$$\varepsilon_{i',j'} = \sum_{k,j} (R^T)_{i',j} \varepsilon_{j,k} R_{k,j'}, \quad (\text{C2})$$

where the Euler matrix reads

$$R = \begin{pmatrix} \cos \theta & 0 & \sin \theta \\ 0 & 1 & 0 \\ -\sin \theta & 0 & \cos \theta \end{pmatrix}. \quad (\text{C3})$$

This matrix describes the rotation of the c axis by an angle θ . In the following we omit prime superscripts in notations, since we do not have $\varepsilon_{i,j}$ in the following equations. Based on the written expressions, we reshape the stress tensor in terms of displacement u using

$$\varepsilon_{i,j} = \frac{1}{2} \left(\frac{\partial u_i}{\partial x_j} + \frac{\partial u_j}{\partial x_i} \right), \quad (\text{C4})$$

where coordinates are denoted as $\{x_x, x_y, x_z\}$. If we write the force density in the form

$$f_i = \sum_j \frac{\partial \sigma_{i,j}}{\partial x_j}, \quad (\text{C5})$$

then Hooke's equation of motion reads

$$\rho \frac{\partial^2 \mathbf{u}}{\partial t^2} + \delta \frac{\partial \mathbf{u}}{\partial t} = \mathbf{f}, \quad (\text{C6})$$

where ρ is the mass density, and $\delta = \eta_a \rho$. The components of the above equation read (for $\theta = 0^\circ$)

$$\begin{aligned}\rho \frac{\partial^2 u_x}{\partial t^2} &= -\eta \frac{\partial u_x}{\partial t} + \frac{1}{2} c_{11} (u_x^{(0,2,0)} + u_y^{(1,1,0)} + 2u_x^{(2,0,0)}) + \frac{1}{2} c_{12} (u_y^{(1,1,0)} - u_x^{(0,2,0)}) \\ &\quad + c_{13} u_z^{(1,0,1)} + c_{44} (u_x^{(0,0,2)} + u_z^{(1,0,1)}) + 2c_{14} (u_x^{(0,1,1)} + u_y^{(1,0,1)} + u_z^{(1,1,0)}), \\ \rho \frac{\partial^2 u_y}{\partial t^2} &= -\eta \frac{\partial u_y}{\partial t} + \frac{1}{2} c_{11} (2u_y^{(0,2,0)} + u_x^{(1,1,0)} + u_y^{(2,0,0)}) + \frac{1}{2} c_{12} (u_x^{(1,1,0)} - u_y^{(2,0,0)}) \\ &\quad + c_{13} u_z^{(0,1,1)} + c_{44} (u_y^{(0,0,2)} + u_z^{(0,1,1)}) - c_{14} (2u_y^{(0,1,1)} + u_z^{(0,2,0)} - 2u_x^{(1,0,1)} - u_z^{(2,0,0)}), \\ \rho \frac{\partial^2 u_z}{\partial t^2} &= -\eta \frac{\partial u_z}{\partial t} + c_{13} (u_y^{(0,1,1)} + u_x^{(1,0,1)}) + c_{14} (-u_y^{(0,2,0)} + 2u_x^{(1,1,0)} + u_y^{(2,0,0)}) \\ &\quad + c_{33} u_z^{(0,0,2)} + c_{44} (u_y^{(0,1,1)} + u_z^{(0,2,0)} + u_x^{(1,0,1)} + u_z^{(2,0,0)}).\end{aligned}\quad (C7)$$

The spatial derivatives are denoted with superscripts, i.e., $u_z^{(1,1,0)} = \frac{\partial^2 u_z}{\partial x \partial y}$, $u_z^{(0,0,2)} = \frac{\partial^2 u_z}{\partial z^2}$, etc. We use the plane-wave ansatz

$$u_{x,y,z} = \tilde{u}_{x,y,z} e^{i(\omega t - \mathbf{k} \cdot \mathbf{r})}. \quad (C8)$$

Next, we focus on standing waves along the thickness of the sapphire; hence the wave vector has only one component $k = k_z = n\pi/L$, where n is the mode number. Thus, Hooke's equation yields a dispersion equation, which can be written in matrix form:

$$\det \begin{pmatrix} a_{11} & a_{12} & a_{13} \\ a_{21} & a_{22} & a_{23} \\ a_{31} & a_{32} & a_{33} \end{pmatrix} = 0, \quad (C9)$$

where

$$\begin{aligned}a_{11} &= c_{44} k^2 \cos(2\theta) + i\omega\eta - \rho\omega^2, \\ a_{12} &= -c_{14} k^2 \sin(\theta), \\ a_{13} &= -c_{44} k^2 \sin(2\theta), \\ a_{21} &= -c_{14} k^2 \sin(\theta) \cos(\theta), \\ a_{22} &= c_{44} k^2 \cos(\theta) + i\eta\omega - \rho\omega^2, \\ a_{23} &= c_{14} k^2 \sin^2(\theta), \\ a_{31} &= (c_{13} - c_{33}) k^2 \sin(\theta) \cos(\theta), \\ a_{32} &= 0, \\ a_{33} &= -k^2 (c_{13} \sin^2(\theta) + c_{33} \cos^2(\theta)) + \rho\omega^2 - i\eta\omega.\end{aligned}\quad (C10)$$

The group velocities of the acoustic waves can be calculated as

$$v_g = \frac{\partial \omega}{\partial k}. \quad (C11)$$

The explicit form of this equation is not elucidative; we therefore turn to numerical results for the exact solution. We find that the velocities of two acoustic waves are almost the same, $v_g \approx 6.17$ km/s, for the parameters listed in Fig. 14(a); the difference between them depends on the deflection angle θ away from the c axis as shown in Fig. 14. For a miscut angle of $\theta = 0.017^\circ$, we obtain $\Delta v \approx 0.5$ m/s in agreement with the

calculations in the main text using the simplified Christoffel equation [40].

2. Cubic crystallographic structure

We employ the same formalism to derive the velocity difference Δv of acoustic waves in an elastic medium with cubic symmetry. In a cubic system, the stress tensor elements are given by [57]

$$\begin{aligned}\sigma_{x,x} &= c_{11} \varepsilon_{x,x} + c_{12} \varepsilon_{y,y} + c_{12} \varepsilon_{z,z}, \\ \sigma_{y,y} &= c_{12} \varepsilon_{x,x} + c_{11} \varepsilon_{y,y} + c_{12} \varepsilon_{z,z}, \\ \sigma_{z,z} &= c_{12} \varepsilon_{x,x} + c_{12} \varepsilon_{y,y} + c_{11} \varepsilon_{z,z}, \\ \sigma_{y,z} &= \sigma_{z,y} = 2c_{44} \varepsilon_{y,z}, \\ \sigma_{x,z} &= \sigma_{z,x} = 2c_{44} \varepsilon_{x,z}, \\ \sigma_{x,y} &= \sigma_{y,x} = 2c_{44} \varepsilon_{x,y}.\end{aligned}\quad (C12)$$

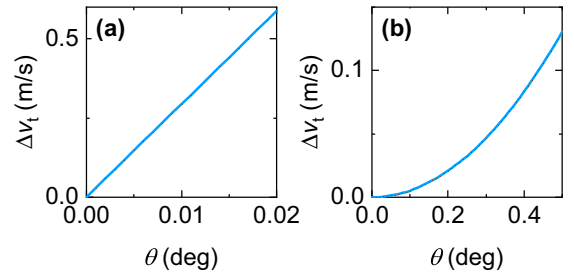


FIG. 14. (a) The difference between velocities of two acoustic waves measured in hexagonal Al_2O_3 . The used parameters are $k = 2\pi/L$ rad m^{-1} , $L = 510$ μm , $\rho = 3970$ kg/m^3 , $c_{11} = 5.00073 \times 10^{11}$ Pa, $c_{33} = 5.02385 \times 10^{11}$ Pa, $c_{44} = 1.51017 \times 10^{11}$ Pa, $c_{12} = 1.61672 \times 10^{11}$ Pa, $c_{13} = 1.11368 \times 10^{11}$ Pa, $c_{14} = -2.32604 \times 10^{10}$ Pa, and $\eta_a/(2\pi) = 0.23$ MHz. These tensor elements are extracted from Ref. [41]. (b) The difference between velocities of two acoustic waves measured in cubic Si. The used parameters are $k = 2\pi/L$ rad m^{-1} , $L = 510$ μm , $\rho = 3970$ kg/m^3 , $c_{11} = 161.8$ GPa, $c_{12} = 64$ GPa, $c_{44} = 76.1$ GPa, and $\eta_a/(2\pi) = 0.23$ MHz. These tensor elements are extracted from Ref. [42].

Performing the same procedure as before, the dispersion equation is given by

$$\det \begin{pmatrix} c_{44}k^2 \cos(2\theta) - \rho\omega^2 + i\delta\omega & 0 & -2c_{44}k^2 \sin(\theta) \cos(\theta) \\ 0 & c_{44}k^2 \cos(\theta) - \rho\omega^2 + i\delta\omega & 0 \\ (c_{11} - c_{12})k^2 \sin(\theta) \cos(\theta) & 0 & c_{12}k^2 \sin^2(\theta) + c_{11}k^2 \cos^2(\theta) - \rho\omega^2 + i\delta\omega \end{pmatrix} = 0. \quad (\text{C13})$$

The calculated Δv solving this equation is plotted in Fig. 14(b).

-
- [1] Y. Chu, P. Kharel, W. H. Renninger, L. D. Burkhardt, L. Frunzio, P. T. Rakich, and R. J. Schoelkopf, Quantum acoustics with superconducting qubits, *Science* **358**, 199 (2017).
- [2] Y. Chu, P. Kharel, T. Yoon, L. Frunzio, P. T. Rakich, and R. J. Schoelkopf, Creation and control of multi-phonon Fock states in a bulk acoustic-wave resonator, *Nature (London)* **563**, 666 (2018).
- [3] C. T. Hann, C.-L. Zou, Y. Zhang, Y. Chu, R. J. Schoelkopf, S. M. Girvin, and L. Jiang, Hardware-efficient quantum random access memory with hybrid quantum acoustic systems, *Phys. Rev. Lett.* **123**, 250501 (2019).
- [4] A. Wallucks, I. Marinković, B. Hensen, R. Stockill, and S. Gröblacher, A quantum memory at telecom wavelengths, *Nat. Phys.* **16**, 772 (2020).
- [5] X. Han, C.-L. Zou, W. Fu, M. Xu, Y. Xu, and H. X. Tang, Superconducting cavity electromechanics: The realization of an acoustic frequency comb at microwave frequencies, *Phys. Rev. Lett.* **129**, 107701 (2022).
- [6] T. P. McKenna, J. D. Witmer, R. N. Patel, W. Jiang, R. Van Laer, P. Arrangoiz-Arriola, E. A. Wollack, J. F. Herrmann, and A. H. Safavi-Naeini, Cryogenic microwave-to-optical conversion using a triply resonant lithium-niobate-on-sapphire transducer, *Optica* **7**, 1737 (2020).
- [7] F. Engelhardt, V. A. S. V. Bittencourt, H. Huebl, O. Klein, and S. V. Kusminskiy, Optimal broadband frequency conversion via a magnetomechanical transducer, *Phys. Rev. Appl.* **18**, 044059 (2022).
- [8] M. Shen, J. Xie, C.-L. Zou, Y. Xu, W. Fu, and H. X. Tang, High frequency lithium niobate film-thickness-mode optomechanical resonator, *Appl. Phys. Lett.* **117**, 131104 (2020).
- [9] W. Jiang, C. J. Sarabalis, Y. D. Dahmani, R. N. Patel, F. M. Mayor, T. P. McKenna, R. Van Laer, and A. H. Safavi-Naeini, Efficient bidirectional piezo-optomechanical transduction between microwave and optical frequency, *Nat. Commun.* **11**, 1166 (2020).
- [10] G. Arnold, M. Wulf, S. Barzanjeh, E. S. Redchenko, A. Rueda, W. J. Hease, F. Hassani, and J. M. Fink, Converting microwave and telecom photons with a silicon photonic nanomechanical interface, *Nat. Commun.* **11**, 4460 (2020).
- [11] A. Bienfait, Y. P. Zhong, H.-S. Chang, M.-H. Chou, C. R. Conner, É. Dumur, J. Grebel, G. A. Peairs, R. G. Povey, K. J. Satzinger, and A. N. Cleland, Quantum erasure using entangled surface acoustic phonons, *Phys. Rev. X* **10**, 021055 (2020).
- [12] V. Jain, V. D. Kurilovich, Y. D. Dahmani, C. U. Lei, D. Mason, T. Yoon, P. T. Rakich, L. I. Glazman, and R. J. Schoelkopf, Acoustic radiation from a superconducting qubit: From spontaneous emission to Rabi oscillations, *Phys. Rev. Appl.* **20**, 014018 (2023).
- [13] P. Delsing, A. N. Cleland, M. J. A. Schuetz, J. Knörzer, G. Giedke, J. I. Cirac, K. Srinivasan, M. Wu, K. C. Balram, C. Bäuerle, T. Meunier, C. J. B. Ford, P. V. Santos, E. Cerda-Méndez, H. Wang, H. J. Krenner, E. D. S. Nysten, M. Weiß, G. R. Nash, L. Thevenard *et al.*, The 2019 surface acoustic waves roadmap, *J. Phys. D: Appl. Phys.* **52**, 353001 (2019).
- [14] K. J. Satzinger, Y. P. Zhong, H.-S. Chang, G. A. Peairs, A. Bienfait, M.-H. Chou, A. Y. Cleland, C. R. Conner, É. Dumur, J. Grebel, I. Gutierrez, B. H. November, R. G. Povey, S. J. Whiteley, D. D. Awschalom, D. I. Schuster, and A. N. Cleland, Quantum control of surface acoustic-wave phonons, *Nature (London)* **563**, 661 (2018).
- [15] C. A. Potts, E. Varga, V. A. S. V. Bittencourt, S. V. Kusminskiy, and J. P. Davis, Dynamical backaction magnomechanics, *Phys. Rev. X* **11**, 031053 (2021).
- [16] M. Aspelmeyer, T. J. Kippenberg, and F. Marquardt, Cavity optomechanics, *Rev. Mod. Phys.* **86**, 1391 (2014).
- [17] A. D. O'Connell, M. Hofheinz, M. Ansmann, R. C. Bialczak, M. Lenander, E. Lucero, M. Neeley, D. Sank, H. Wang, M. Weides, J. Wenner, J. M. Martinis, and A. N. Cleland, Quantum ground state and single-phonon control of a mechanical resonator, *Nature (London)* **464**, 697 (2010).
- [18] M. Goryachev, D. L. Creedon, E. N. Ivanov, S. Galliou, R. Bourquin, and M. E. Tobar, Extremely low-loss acoustic phonons in a quartz bulk acoustic wave resonator at millikelvin temperature, *Appl. Phys. Lett.* **100**, 243504 (2012).
- [19] M. Goryachev, Z. Kuang, E. N. Ivanov, P. Haslinger, H. Muller, and M. E. Tobar, Next generation of phonon tests of Lorentz invariance using quartz BAW resonators, *IEEE Trans. Ultrason. Ferroelect. Freq. Contr.* **65**, 991 (2018).
- [20] G. Andersson, S. W. Jolin, M. Scigliuzzo, R. Borgani, M. O. Tholén, J. C. Rivera Hernández, V. Shumeiko, D. B. Haviland, and P. Delsing, Squeezing and multimode entanglement of surface acoustic wave phonons, *PRX Quantum* **3**, 010312 (2022).
- [21] M. K. Ekström, T. Aref, J. Runeson, J. Björck, I. Boström, and P. Delsing, Surface acoustic wave unidirectional transducers for quantum applications, *Appl. Phys. Lett.* **110**, 073105 (2017).
- [22] K. An, A. N. Litvinenko, R. Kohno, A. A. Fuad, V. V. Naletov, L. Vila, U. Ebels, G. de Loubens, H. Hurdequint, N. Beaulieu, J. Ben Youssef, N. Vukadinovic, G. E. W. Bauer, A. N. Slavin, V. S. Tiberkevich, and O. Klein, Coherent long-range transfer of angular momentum between magnon Kittel modes by phonons, *Phys. Rev. B* **101**, 060407(R) (2020).
- [23] K. An, R. Kohno, A. N. Litvinenko, R. L. Seeger, V. V. Naletov, L. Vila, G. de Loubens, J. Ben Youssef, N. Vukadinovic, G. E. W. Bauer, A. N. Slavin, V. S. Tiberkevich, and O. Klein, Bright and dark states of two distant macrospins strongly coupled by phonons, *Phys. Rev. X* **12**, 011060 (2022).
- [24] B. Flebus, K. Shen, T. Kikkawa, K.-I. Uchida, Z. Qiu, E. Saitoh, R. A. Duine, and G. E. W. Bauer, Magnon-polaron transport in magnetic insulators, *Phys. Rev. B* **95**, 144420 (2017).

- [25] S. Sharma, V. S. V. Bittencourt, and S. V. Kusminskiy, Protocol for generating an arbitrary quantum state of the magnetization in cavity magnonics, *J. Phys. Mater.* **5**, 034006 (2022).
- [26] V. A. S. V. Bittencourt, I. Liberal, and S. Viola Kusminskiy, Optomagnonics in dispersive media: Magnon-photon coupling enhancement at the epsilon-near-zero frequency, *Phys. Rev. Lett.* **128**, 183603 (2022).
- [27] V. Wachter, V. A. S. V. Bittencourt, S. Xie, S. Sharma, N. Joly, P. S. J. Russell, F. Marquardt, and S. V. Kusminskiy, Optical signatures of the coupled spin-mechanics of a levitated magnetic microparticle, *J. Opt. Soc. Am. B* **38**, 3858 (2021).
- [28] R. Schlitz, L. Siegl, T. Sato, W. Yu, G. E. W. Bauer, H. Huebl, and S. T. B. Goennenwein, Magnetization dynamics affected by phonon pumping, *Phys. Rev. B* **106**, 014407 (2022).
- [29] S. Streib, H. Keshtgar, and G. E. W. Bauer, Damping of magnetization dynamics by phonon pumping, *Phys. Rev. Lett.* **121**, 027202 (2018).
- [30] T. Sato, W. Yu, S. Streib, and G. E. W. Bauer, Dynamic magnetoelastic boundary conditions and the pumping of phonons, *Phys. Rev. B* **104**, 014403 (2021).
- [31] D. Hatanaka, M. Asano, H. Okamoto, Y. Kunihashi, H. Sanada, and H. Yamaguchi, On-chip coherent transduction between magnons and acoustic phonons in cavity magnomechanics, *Phys. Rev. Appl.* **17**, 034024 (2022).
- [32] W. K. Peria, D.-L. Zhang, Y. Fan, J.-P. Wang, and P. A. Crowell, Anomalous temperature dependence of phonon pumping by ferromagnetic resonance in Co/Pd multilayers with perpendicular anisotropy, *Phys. Rev. B* **106**, L060405 (2022).
- [33] H. Keshtgar, M. Zareyan, and G. E. W. Bauer, Acoustic parametric pumping of spin waves, *Solid State Commun.* **198**, 30 (2014).
- [34] M. Weiler, L. Dreher, C. Heeg, H. Huebl, R. Gross, M. S. Brandt, and S. T. B. Goennenwein, Elastically driven ferromagnetic resonance in nickel thin films, *Phys. Rev. Lett.* **106**, 117601 (2011).
- [35] M. Weiler, H. Huebl, F. S. Goerg, F. D. Czeschka, R. Gross, and S. T. B. Goennenwein, Spin pumping with coherent elastic waves, *Phys. Rev. Lett.* **108**, 176601 (2012).
- [36] N. W. Ashcroft and D. N. Mermin, *Solid State Physics* (Oldenbourg Wissenschaftsverlag, 2012).
- [37] R. Gross and A. Marx, *Festkörperphysik* (De Gruyter Oldenbourg, Berlin, 2022).
- [38] J. P. Wolfe, *Imaging Phonons* (Cambridge University Press, Cambridge, UK, 1998).
- [39] F. I. Fedorov, *Theory of Elastic Waves in Crystals* (Springer, Boston, 1968).
- [40] J. W. Jaeken and S. Cottenier, Solving the Christoffel equation: Phase and group velocities, *Comput. Phys. Commun.* **207**, 445 (2016).
- [41] W. E. Tefft, Elastic constants of synthetic single crystal corundum, *J. Res. Natl. Bur. Stan. Sect. A* **70A**, 277 (1966).
- [42] C. Malica and A. D. Corso, Quasi-harmonic temperature dependent elastic constants: Applications to silicon, aluminum, and silver, *J. Phys.: Condens. Matter* **32**, 315902 (2020).
- [43] E. R. J. Edwards, H. T. Nembach, and J. M. Shaw, Co₂₅Fe₇₅ Thin films with ultralow total damping of ferromagnetic resonance, *Phys. Rev. Appl.* **11**, 054036 (2019).
- [44] L. Flacke, L. Liensberger, M. Althammer, H. Huebl, S. Geprägs, K. Schultheiss, A. Buzdakov, T. Hula, H. Schultheiss, E. R. J. Edwards, H. T. Nembach, J. M. Shaw, R. Gross, and M. Weiler, High spin-wave propagation length consistent with low damping in a metallic ferromagnet, *Appl. Phys. Lett.* **115**, 122402 (2019).
- [45] M. A. W. Schoen, D. Thonig, M. L. Schneider, T. J. Silva, H. T. Nembach, O. Eriksson, O. Karis, and J. M. Shaw, Ultra-low magnetic damping of a metallic ferromagnet, *Nat. Phys.* **12**, 839 (2016).
- [46] H. Maier-Flaig, S. T. B. Goennenwein, R. Ohshima, M. Shiraishi, R. Gross, H. Huebl, and M. Weiler, Note: Derivative divide, a method for the analysis of broadband ferromagnetic resonance in the frequency domain, *Rev. Sci. Instrum.* **89**, 076101 (2018).
- [47] D. Schwienbacher, M. Pernpeintner, L. Liensberger, E. R. J. Edwards, H. T. Nembach, J. M. Shaw, M. Weiler, R. Gross, and H. Huebl, Magnetoelasticity of Co₂₅Fe₇₅ thin films, *J. Appl. Phys.* **126**, 103902 (2019).
- [48] P. F. Herskind, A. Dantan, J. P. Marler, M. Albert, and M. Drewsen, Realization of collective strong coupling with ion Coulomb crystals in an optical cavity, *Nat. Phys.* **5**, 494 (2009).
- [49] H. Huebl, C. W. Zollitsch, J. Lotze, F. Hocke, M. Greifenstein, A. Marx, R. Gross, and S. T. B. Goennenwein, High cooperativity in coupled microwave resonator ferrimagnetic insulator hybrids, *Phys. Rev. Lett.* **111**, 127003 (2013).
- [50] X. Zhang, C.-L. Zou, L. Jiang, and H. X. Tang, Strongly coupled magnons and cavity microwave photons, *Phys. Rev. Lett.* **113**, 156401 (2014).
- [51] Y. Minami, T. Yogi, and K. Sakai, Thermal phonon resonance in solid glass, *Jpn. J. Appl. Phys.* **45**, 4469 (2006).
- [52] M. Born, E. Wolf, A. B. Bhatia, P. C. Clemmow, D. Gabor, A. R. Stokes, A. M. Taylor, P. A. Wayman, and W. L. Wilcock, *Principles of Optics* (Cambridge University Press, Cambridge, UK, 1999).
- [53] I. E. Psarobas, D. A. Exarchos, and T. E. Matikas, Birefringent phononic structures, *AIP Adv.* **4**, 124307 (2014).
- [54] S. M. Bakharev, M. A. Borich, and S. P. Savchenko, Features of focusing magnetoelastic waves in YIG crystals, *J. Phys.: Conf. Ser.* **1389**, 012096 (2019).
- [55] E. Klokholm and J. Aboaf, The saturation magnetostriction of thin polycrystalline films of iron, cobalt, and nickel, *J. Appl. Phys.* **53**, 2661 (1982).
- [56] M. Yamamoto, Young's modulus of elasticity and its change with magnetization in iron-cobalt alloys, *Phys. Rev.* **59**, 768 (1941).
- [57] J. F. Nye *et al.*, *Physical Properties of Crystals* (Oxford University Press, Oxford, UK, 1985).